JACS
JOURNAL OF THE AMERICAN CHEMICAL SOCIETY
pubs.acs.org/JACS

Article

Chemostructurally Stable Polyionomer Coatings Regulate Proton-Intermediate Landscape in Acidic CO_2 Electrolysis

Bárbara Polesso, Adrián Pinilla-Sánchez, Eman H. Ahmed, Anku Guha, Marinos Dimitropoulos, Blanca Belsa, Viktoria Golovanova, Lu Xia, Ranit Ram, Sunil Kadam, Aparna M. Das, Junmei Chen, Johann Osmond, Adam Radek Martínez, Melanie Micali, Esther Alarcón Lladó, and F. Pelayo García de Arquer*

Cite This: J. Am. Chem. Soc. 2025, 147, 27278−27288

Read Online

ACCESS | Metrics & More | Article Recommendations | Supporting Information

ABSTRACT: CO_2 electroreduction (CO_2R) in acidic media offers a path to high carbon utilization via local carbonate regeneration. However, this proton-rich environment challenges achieving a combined selectivity and rate toward multicarbon (C_{2+}) products due to proton and intermediate competition. Here, we demonstrate a strategy to modulate local protons and intermediates, at these settings, using a polyionomer coating over benchmark copper gas diffusion electrodes. The polyionomer integrates amine ($-NH_x$) function from branched polyethylenimine (PEI) with sulfonate ($-SO_3^-$) and amphiphilic functions from PFSA. We show that their chemical structure enables H-bonding interaction, leading to a stereochemical assembly that retains a structure−property relationship through a wide pH range (2−14). PFSA domains modulate *CO intermediates and local $[CO_2]/[H_2O]$ and K^+ environment, while partially protonated amines provide further control over proton availability and intermediate stabilization, which in combination enhance C−C coupling. When implemented in a flow cell (0.5 M K_2/H_2SO_4, pH = 2), the optimized polyionomer coating enables a C_{2+} Faradaic efficiency of 61% at a single-pass CO_2 utilization of 84%, including a conversion efficiency of 64% toward C_{2+}, at a current density of at 0.3 A cm^{-2}—an improvement of almost 30% in C_{2+} selectivity and 35% in carbon utilization compared to monofunctional coatings. These findings expand the toolbox of strategies to modulate CO_2R microenvironments toward improved performance.

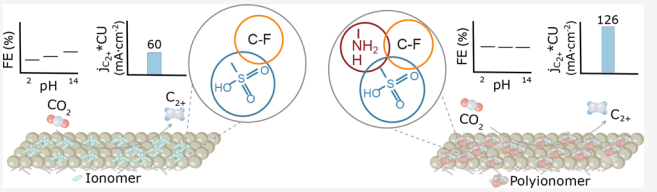

INTRODUCTION

Electrochemical CO_2 reduction (CO_2R) offers a path to mitigate global greenhouse emissions by converting atmospheric and waste CO_2 into widely used chemicals such as syngas, formic acid, methane, ethanol, and ethylene, among others, using renewable and low carbon electricity.[1−5]

Among these molecules, ethylene and ethanol (multicarbon, C_2 products) are attractive in view of their industrial relevance and potential carbon footprint reduction.[6] Ethylene is widely used as a precursor in the polymer industry and stands out as the largest market size and most valuable product, contributing as the primer product to CO_2 emissions. Ethanol has a high volumetric energy density and can be incorporated into existing fuel supply chains.[1,4−7] Further progress in the performance toward these are still necessary to approach technoeconomic viability.[4−6,8]

Best performance toward C_2 products has been consistently achieved using copper gas diffusion electrodes. Initial progress in alkaline catholytes[3,9−12] was shown to be impractical due to the spontaneous consumption of CO_2 by OH^- into (bi)carbonates, limiting carbon conversion efficiencies (<5%) and overall process viability.[13−15]

This prompted the search for alternatives such as operation in neutral membrane electrode assemblies (MEA), tandem reaction schemes, and carbonate regeneration via local proton replenishment.[16−19] The latter can be implemented using reversely biased bipolar membranes[20] or, directly, by operating CO_2R in acid media.[13,14,21−27] In such a configuration, (bi)carbonates would be converted back to CO_2 by reacting with protons replenished from the anode.[14,25] This, however, favors the competing hydrogen evolution reaction (HER), limiting CO_2R rates (Figure 1a).[13,14,21−26]

Initial progress to overcome this competition largely relied on local pH control. This happens naturally at increasing current densities: as protons get consumed, and their transport is increasingly limited, the proton source shifts from hydronium to water, leading to higher local pH. This may enable CO_2R

Received: January 22, 2025
Revised: July 14, 2025
Accepted: July 15, 2025
Published: July 29, 2025

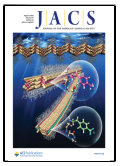

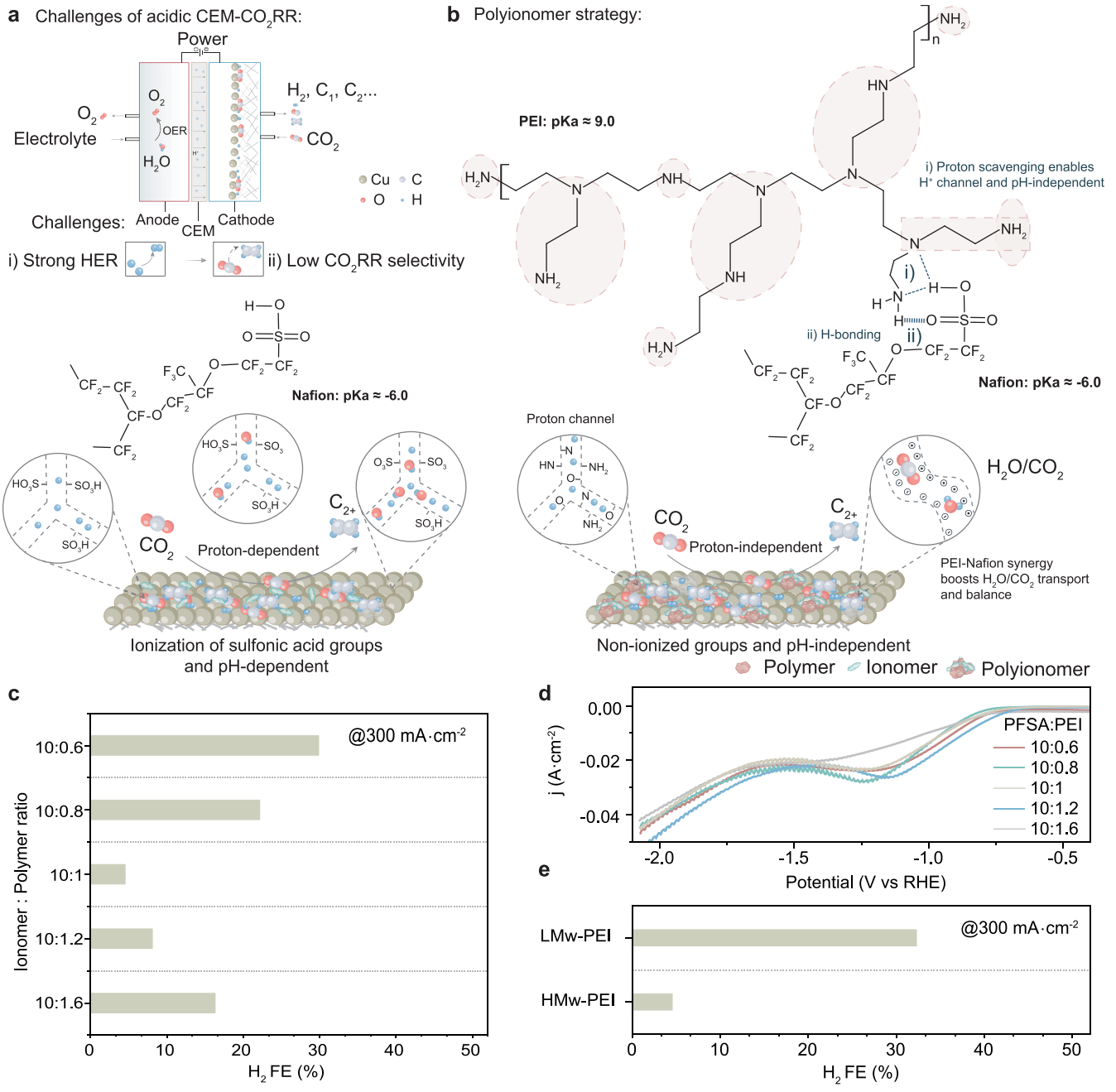

Figure 1. Polyionomer coatings retain chemostructural function in acid to jointly address local protons and CO_2R intermediates. (a) CO_2R challenges and mechanism in acidic media. (b) Chemical structure, orientation, and pK_a values contribute to maintaining the optimal structure−property function of the polyionomer across a wide range of pH values. This is attributed to the presence of proton channels, hydrogen bonding, and $[CO_2]/[H_2O]$ balance which are absent in Cu/ionomer coatings. The highlighted regions in PEI indicate interactions between branched PEI (9) and PFSA (1). (c) Hydrogen Faradaic efficiency (FE) of different ionomer:polymer ratios. (d) Linear sweep voltammetry (LSV) curves indicating proton barrier effect of different ratios of branched PEI with Ar (40 mL min^{-1}) and scan rate of 50 mV s^{-1}. (e) Hydrogen Faradaic efficiency (FE) of Cu/polyionomer with low (LMw-PEI) and high (HMw-PEI) molecular weights of PEI.

depending on the reaction environment.[14,27−29] In neutral and alkaline electrolytes, the local microenvironment can be tuned in the electrode−electrolyte interface using different organic coatings, manipulating CO_2R intermediates and product distribution.[25,26,30−34] For example, amine-functionalized polymers may act as local proton scavengers and CO_2 concentrators, boosting C_{2+} product yields on copper gas diffusion electrodes.[35−37]

However, we posited that surface modification strategies developed for alkaline and neutral CO_2R may not be directly applicable to acidic electrolytes. In neutral and alkaline media, polymer/polyionomer modifiers have been primarily optimized to control OH^- diffusion, enhance CO_2 concentration, and tune hydrophobicity.[38,39] Crucially, these designs do not directly address local proton activity, which under acidic conditions becomes the dominant factor driving competitive HER. Without a mechanism to buffer or regulate proton access at the catalyst interface, conventional coatings lose efficacy and selectivity in acid-fed CO_2R.

https://doi.org/10.1021/jacs.5c01314
J. Am. Chem. Soc. 2025, 147, 27278−27288

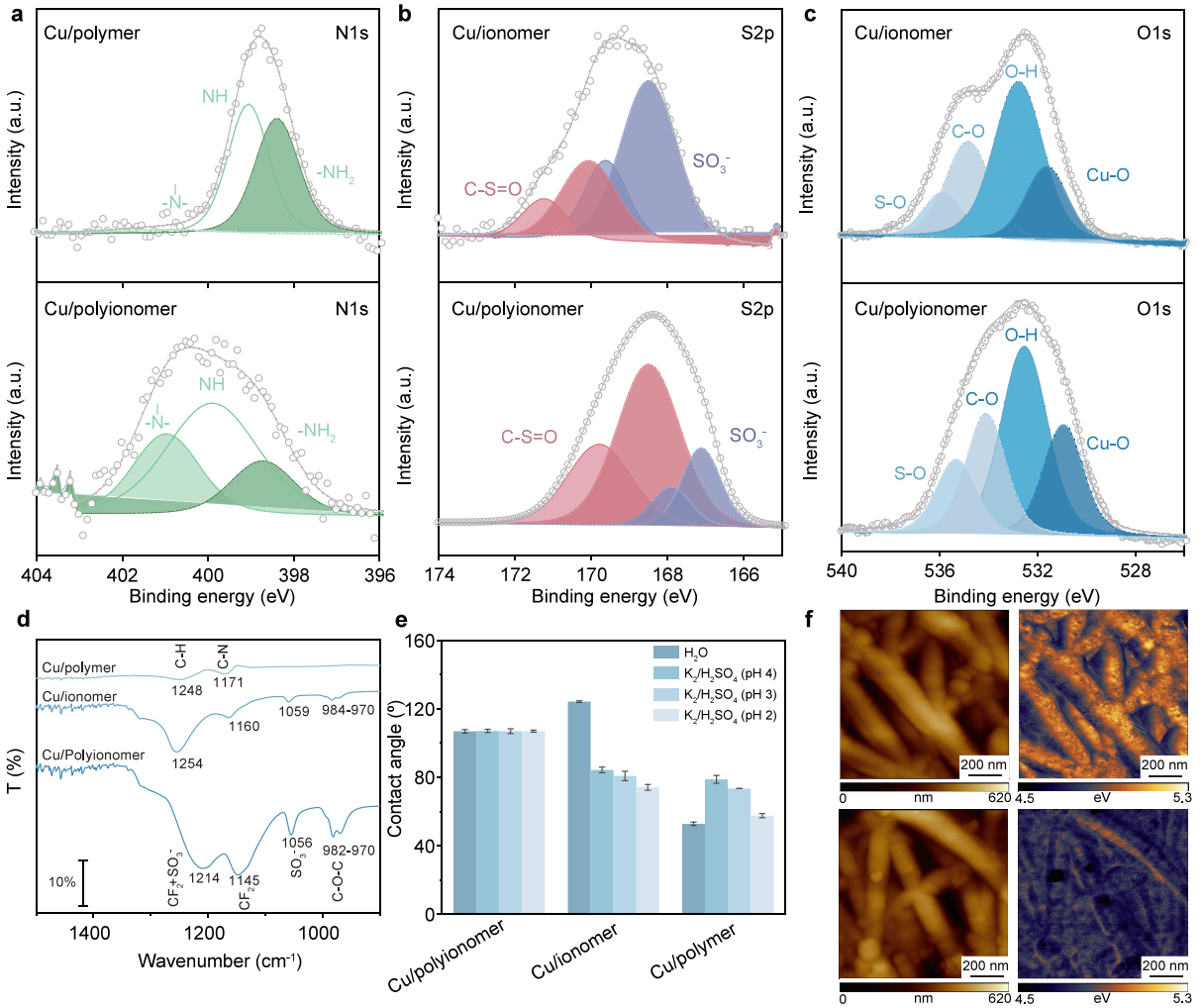

Figure 2. Polyionomer coated electrode characterization. Changes in electron charge density and chemical environment suggest the protonation of amine groups and interaction with sulfonic groups (a) N 1s binding energies shift to higher binding energies when comparing Cu/polyionomer with Cu/polymer. (b) S 2p shift to lower binding energies when comparing Cu/polyionomer with Cu/ionomer. (c) O 1s shift to lower binding energies when comparing Cu/polyionomer with Cu/ionomer. (d) ATR-FTIR of Cu/ionomer, Cu/polymer, and Cu/polyionomer characteristic bands between 1600 and 900 cm^{-1}. Characteristic peaks for Cu/polymer and Cu/ionomer at 1248 cm^{-1} (C−H), 1171 cm^{-1} (C−N), 1254 cm^{-1} (CF_2 + SO_3^-) and 1160 cm^{-1} (CF_2) shift to 1214 cm^{-1} and 1145 cm^{-1} in the polyionomer sample. (e) Contact angle comparison in a wide pH range for Cu/polymer, Cu/ionomer and Cu/polyionomer. (f) Representative topography with respective work function maps highlighting the changes in the surface potential between Cu/ionomer (top) and Cu/polyionomer (bottom).

To overcome these challenges, recent approaches such as cation-group augmentation and organic thin films have separately demonstrated control over proton-flux, mitigation or intermediate stabilization in strongly acidic CO_2R.[27,29,31,40]

We hypothesized that the high proton concentration and distinct ionic environment in acid may not only alter reaction pathways—favoring hydrogen evolution over CO_2R—but also disrupt structure−property−function relationships of polymer coatings. Our preliminary results revealed varying hydrophobicity of PFSA coatings as a function of pH (Figure S1), which could be compatible with this picture.

To bridge this gap, we sought to design a chemostructurally stable coating capable of "locking in" multifunctionality across the wide pH swings characteristic of acid-fed CO_2R. To this end, we turned our attention to PFSA ionomers (e.g., Nafion) and branched polyethylenimine (PEI). The former, in view of their ability to improve CO_2R by virtue of cation concentration and water management; the latter, because of their wide primary, secondary, and tertiary amine functions.

In acidic conditions, the protonation ratio of amine groups is higher compared to that in neutral and alkaline pHs.[41] We hypothesized that this could enable function beyond conventional CO_x stabilization, as the interaction of amines with $-SO_3^-$ groups could be harnessed to control ionomer assembly and structure−property function in acid.

Owing to the chemical structure, orientation, and pK_a values, the amine groups in PEI (p$K_a \approx 9.0$)[42] and $-SO_3H$ group of PFSA (p$K_a \approx -6$)[43] via proton scavenging form a stable and favorable 5-membered ring structure along with H-bonding in specific branched positions (Figure 1b). Thus, the polyionomer structure stabilizes in a typical 1:9 ratio of PEI and PFSA. Unlike for monofunctional coatings, which show a highly pH-sensitive CO_2R product distribution, polyionomers retain HER suppression within pH 2−14 (Figure S2). The optimized polyionomer coatings (PEI and PFSA in 1:10) implemented over benchmark poly(tetrafluoroethylene) (PTFE)/polycrystalline copper gas diffusion electrodes further enable the simultaneous control over *CO intermediates and reaction modulators ($[CO_2]/[H_2O]$

https://doi.org/10.1021/jacs.5c01314
J. Am. Chem. Soc. 2025, 147, 27278−27288

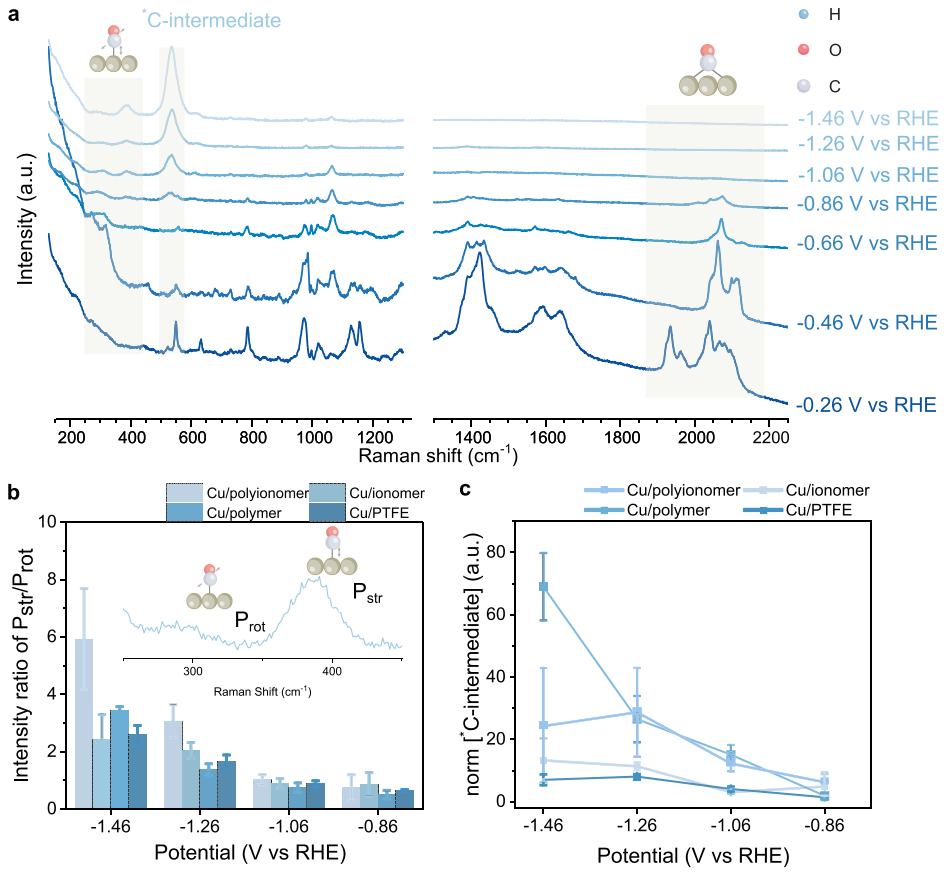

Figure 3. In situ Raman spectroscopy studies. (a) Raman spectrum of Cu/polyionomer sample in different applied potentials (V vs RHE) labeling corresponding intermediates or species, highlighting *CO and *C-intermediates. Samples were taken in 0.5 M K_2SO_4 (pH 2) in a flow cell under working potentials. (b) *CO coverage potential dependence correlation with the intensity ratio P_{str}/P_{rot} of Cu/PTFE, Cu/ionomer, Cu/polymer, and Cu/polyionomer. (c) Normalized *C-intermediate area comparison between Cu/PTFE, Cu/ionomer, Cu/polymer, and Cu/polyionomer.

and CO_2 potassium activation), supported by in situ Raman spectroscopy.

When implemented in a flow cell (0.5 M K_2/H_2SO_4, pH = 2), they achieve a single pass CO_2 conversion of 84% at industrially relevant current densities (0.3 A cm^{-2}) and selective C_{2+} production of 61%. This represents an improvement of almost 30% in C_{2+} selectivity and 35% in carbon utilization compared with conventional monofunctional coatings.

RESULTS

We began by assessing the effect of PEI (polymer) incorporation on H_2 suppression for a fixed amount of PFSA (ionomer) and loading. Scanning electron micrographs (SEM-EDX) and atomic force microscopy (AFM) revealed a homogeneous coating of PSFA-PEI binders over the entire catalyst surface (Figures S3−S5). An ionomer:polymer ratio of 10:1 results in a significant suppression of H_2 generation at 0.3 A cm^{-2} (Figure 1c and Figure S6). Polarization curves (Figure 1d) indicate a proton barrier effect depending on ionomer:polymer ratio, revealing a depletion of H_3O^+ at lower currents for 10:1 compared to others.[29]

To address how the amount of amine groups could interfere in CO_2 activation and hydrogen bonding close to the surface,[30] we further compared the extent of HER suppression for branched high and low molecular weight (Mw) polyethylenimine (PEI). HER was more suppressed with high Mw PEI (HMw-PEI) (Figure 1e and Figure S7), which could be correlated with a thicker proton-resistant layer due to a larger number of repeating units.[44]

To assess the individual role of the polymer and ionomer on microenvironment modulation, we prepared three different electrode configurations: two in a bilayer configuration (copper/polymer/ionomer and copper/ionomer/polymer) and one copper/polyionomer (Figure S8).

Comparing again the H_2 selectivity at 0.3 A cm^{-2} (Figure S9), the polyionomer shows the highest H_2 suppression (Figure S9). Both bilayer configurations also suggest the presence of regions with high local acid penetration, allowing the HER to dominate the overall reaction, probably blocking the diffusion of CO_2 to desired products. This is supported by the plateau of HER current in the bilayer configuration (Figure S10).

To get more insights on the chemical configuration of the polyionomer, the interaction between their functional groups, and structure−property function, we performed a combination of X-ray photoelectron spectroscopy (XPS), attenuated total reflectance-Fourier transform infrared (ATR-FTIR), contact angle, and atomic force microscopy (AFM)/Kelvin probe force microscopy (KPFM) (Figure 2) measurements.

Shifts in the positions of XPS peaks can relate to interactions occurring due to changes in the electron density and chemical environment. We observed higher binding energies in N 1s XPS peaks in the Cu/polyionomer compared to the bare Cu/polymer coatings and lower binding energies in the Cu/polyionomer compared to the bare Cu/ionomer coatings (Figure 2a and Tables S1−S3). Concurrently, lower binding

https://doi.org/10.1021/jacs.5c01314
J. Am. Chem. Soc. 2025, 147, 27278−27288

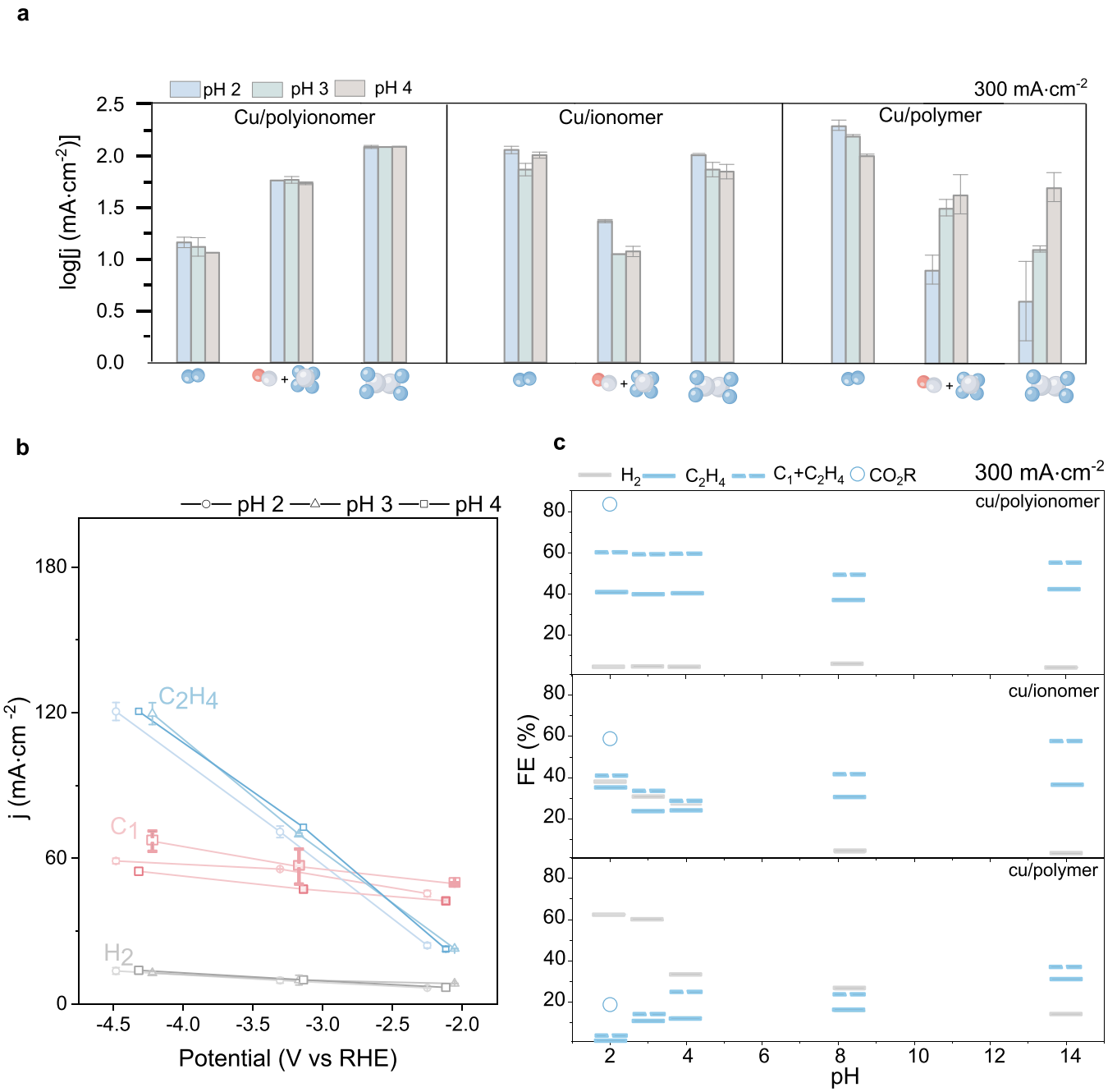

Figure 4. Selectivity of CO_2 electroreduction study via electrolyte pH change. (a) Logarithm of partial current density for gas product distribution of Cu/polyionomer, Cu/ionomer, and Cu/polymer at 300 mA cm^{-2} showing pH-independence of polyionomer. (b) Cu/polyionomer partial current density of CO_2 gas products vs potential (V vs RHE). (c) Gas product distribution at 300 mA cm^{-2} in a wider pH range up to alkaline conditions (acid, 0.5 M K_2SO_4: pH 2, pH 3 and pH 4; neutral, 1 M $KHCO_3$; alkaline, 1 M KOH) and total products of CO_2R at pH 2. Cu/polyionomer maintains C_2H_4 selectivity comparable to that of Cu/ionomer under alkaline conditions but outperforms it as pH decreases, unlike Cu/ionomer and Cu/polymer, which exhibit increased HER and reduced C−C coupling in acidic environments. This supports the suggested distinctive character of the polyionomer in preserving PFSA functionality while enabling local $[H^+]$ and CO regulation through PEI, thereby facilitating C−C coupling. FE (%) denotes Faradaic efficiency.

energy shifts are observed in S 2p (directly) and O 1s (indirectly) XPS peaks in Cu/polyionomer, when compared to Cu/ionomer (Figure 2b,c). These complementary shifts suggest the electronic and chemical interaction between PEI and PFSA as a form of proton scavenging, transfer of electronic charge density, and H-bonding when assembled on Cu/PTFECu. We observe a similar trend in ATR-FTIR spectra (Figure 2d), showing in Cu/polyionomer shifts in characteristic peaks of perfluorosulfonic groups and carbon−nitrogen bonds.[9,45−47]

To gain more insights into the polyionomer function, we performed contact angle measurements (Figure 2e). The similar contact angle across a wide pH range suggests that the polyionomer most exposed function (and structure) does not change drastically with pH,[48] as opposed to individual PFSA and PEI contact angle trends, remaining comparable to the initial contact angle of PFSA at high pH. This indicates that the

https://doi.org/10.1021/jacs.5c01314
J. Am. Chem. Soc. 2025, 147, 27278−27288

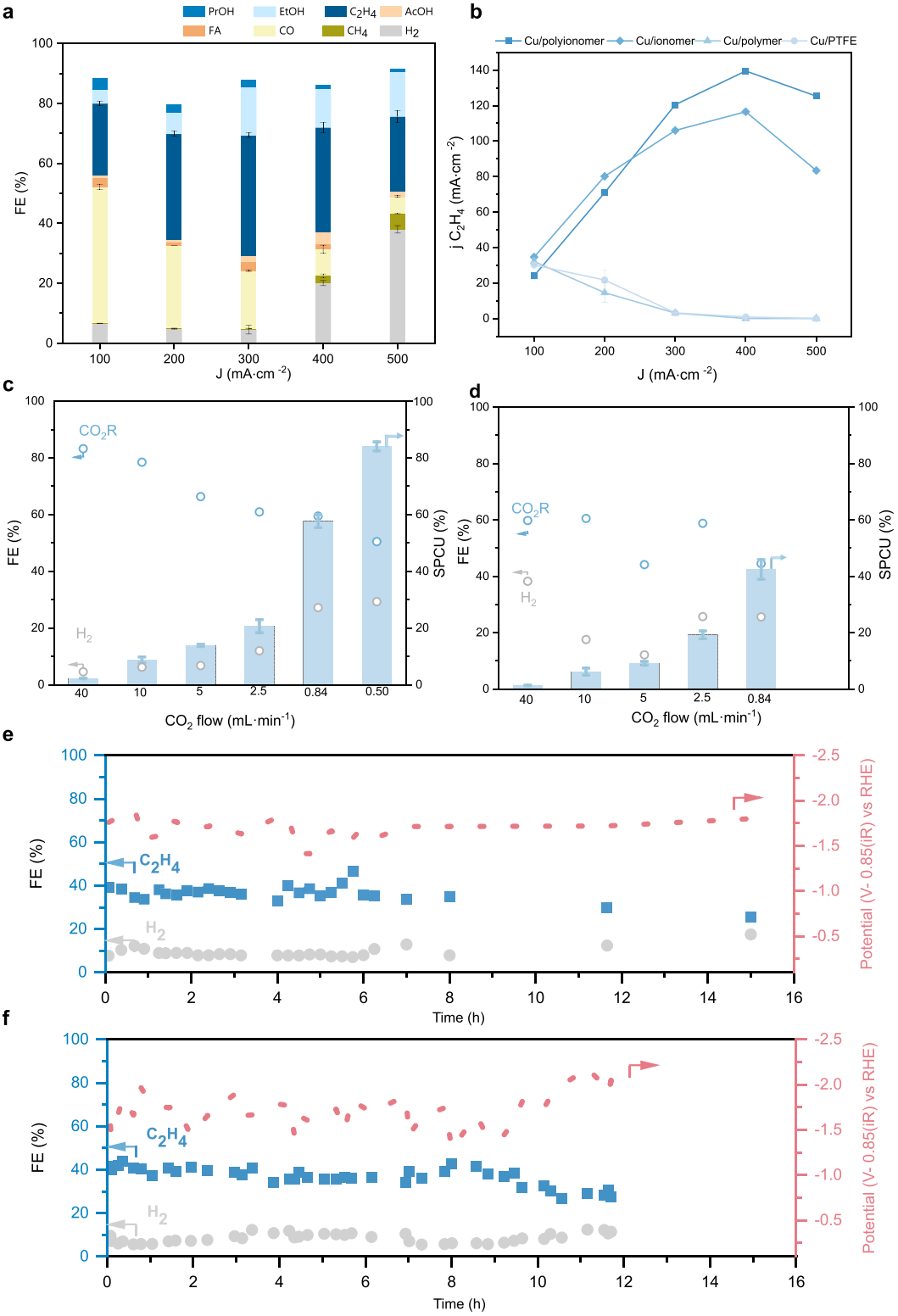

Figure 5. Electrocatalytic performance in 0.5 M H_2/K_2SO_4(pH 2) in a flow cell. (a) Product distribution of Cu/polyionomer in the current range 0.1−0.5 A cm^{-2}. FE (%) denotes Faradaic efficiency. Values are means, and error bars indicate SD (n = 3 replicates). (b) Ethylene partial current density of Cu/polyionomer compared with controls (Cu, Cu/ionomer, and Cu/polymer). (c) Single pass conversion of CO_2 at different flow rates for Cu/polyionomer. (d) Single pass conversion of CO_2 at different flow rates for Cu/ionomer. The SPCU results were obtained at a constant current density of 0.3 A cm^{-2} and an improvement of 35% in carbon utilization is observed when comparing Cu/polyionomer with Cu/ionomer. (e) Cu/polyionomer retains performance during 16 h of pulsed electrolysis at 0.3 A cm^{-2}. (f) Continuous stability of Cu/polyionomer coated with Vulcan carbon at 0.3 A cm^{-2}. The lifetime is extended to 24 h at 0.1 A cm^{-2} (Figure S24).

resulting structure could take better advantage of the hydrophobic channels in Cu/ionomer to offset $[CO_2]/[H_2O]$ balance, as opposed to overexpressing the hydrophilic channels of branched polyamines.[30]

https://doi.org/10.1021/jacs.5c01314
J. Am. Chem. Soc. 2025, 147, 27278−27288

To assess the impact of the polyionomer on the electrostatic environment,[49,50] we measured the work function combined with atomic force microscopy of the coated gas diffusion electrodes. Cu/polyionomer (4.60 ± 0.05 eV) showed a decrease in work function compared with Cu/ionomer (4.85 ± 0.1 eV) (Figure 2f). This shift, combined with the charge re-equilibration observed in XPS and FTIR, further suggests the modification of the ionomer arrangement and chemical function.

To understand the role of polyionomer in controlling the electrode−electrolyte microenvironment, we performed in situ surface-enhanced Raman spectroscopy (SERS) in the region of −0.26 to −1.46 V vs RHE in two regions: R_1 (100−1250 cm^{-1}), highlighting Cu-*CO and *C-intermediates, and R_2 (1300−2250 cm^{-1}), highlighting *CO intermediates (Figure 3a).[51,52]

The intensity ratio of Cu-*CO frustrated rotation (P_{rot}, 295−303 cm^{-1}) and Cu-*CO stretching vibration (P_{str}, 382−389 cm^{-1}) often correlated with *CO coverage (Figure 3b and Figures S14−S17).[53−56] These ratios increase for all of the catalysts, indicating that the *CO coverage increases with increasing applied potential (Figure 3b). The observed highest intensity ratio for polyionomer may indicate the highest CO_2R activity of polyionomer among all the catalysts.

Carbon intermediate (*C-intermediate) (Figure 3c) is another important factor to directly correlate to CO_2 reduction to C_{2+} products.[57−59] At higher applied potential (−1.46 V vs RHE), both Cu/polyionomer and Cu/polymer show stronger *C-intermediate bands compared to Cu/ionomer and Cu/PTFE. The stabilization of *C-intermediates could be influenced by variations in electronic charge distribution and can be modulated by the presence of amine groups.[60,61] This effect is supported by AFM/KPFM data, which suggest that the presence of PEI contributes to stabilizing this intermediate by a decrease in work function observed between the Cu/ionomer and Cu/polyionomer (Figures 2f and 3c). Further, CO_2^- and *CO_2 (Figure S15) species are observed in Cu/polymer, which may be correlated with enhanced CO_2 adsorption and activation on active sites.[62] This indicates that polyethylenimine (PEI) plays a crucial role in stabilizing intermediates and accelerating reaction pathways through hydrogen bonding and interactions with nearby active sites.[63] However, these favorable thermodynamic effects alone do not translate into higher performance, as efficient CO_2 reduction also relies on optimized reaction kinetics.[64]

To assess potential changes in kinetics derived from polyionomer coatings, we tracked the carbonate band (∼1062 cm^{-1}) by in situ surface enhanced Raman spectroscopy. PFSA polymers have demonstrated improved performance in acidic media by accumulating alkali cations near the catalyst interface and buffering the local pH.[14,65,66] The carbonate band is more intense in Cu/polyionomer compared to Cu/polymer and Cu/ionomer (Figures S14−S17) suggesting a local higher alkalinity and CO_2 availability for Cu/polyionomer. However, due to the presence of multiple bands in this region, accurate deconvolution remains challenging.

To further understand how the polyionomer could regulate local proton activity and the reaction mechanism, we characterized selectivity at different pH and fixed current densities (Figure 4a). HER rejection and selectivity within gas products remain similar regardless of electrolyte pH for Cu/polyionomer (Figure 4b and Figure S18), whereas they vary for both ionomer and polymer samples (Figure 4a). Such pH independence is in line with contact angle measurements and could be associated with a balanced proportion of $[CO_2]/[OH^-]$ (from PFSA) that compensate the mass transfer of protons to the electrode surface,[67−71] combined with the buffering of local protons and *CO intermediate stabilization (from PEI) consistent with SERS.[72] Consistently across all tested pH values, Cu/polyionomer electrodes require a lower potential vs SHE (standard hydrogen electrode) than either Cu/ionomer or Cu/polymer to sustain similar CO_2R product generation (Figure S19).

To interrogate polyionomer function, we studied gas product distribution in a wider pH range up to alkaline conditions (Figure 4c and Figure S2). Cu/polyionomer electrodes exhibit a similar H_2 rejection and C−C coupling across the 2−14 pH range (Figure 4c and Figure S2). Cu/polyionomer shows selectivity comparable to that of the single-function Cu/ionomer at high pH. The latter shows, on the other hand, increasing HER and reducing C−C coupling as the pH decreases into the acid regime. Cu/polymer exhibits a trend similar to that of Cu/ionomer with exacerbated HER and lowered C−C selectivity. This supports the suggested distinctive character of the polyionomer retaining PFSA function and further allowing control over $[H^+]$ and *CO to promote C−C coupling via PEI.

To further assess the generalizability of this strategy, we performed similar electrochemical performance tests at different pH levels by using PTFE/Ag electrodes. These also reveal a pH-independent trend in Ag/polyionomer electrodes compared to Ag/ionomer electrodes (Figure S20).

We assessed the electrochemical performance of Cu/polyionomer electrodes in a flow cell at different current densities and pH 2 (Figure 5a). The maximum ethylene Faradaic efficiency was 40.1% (±0.8), with a combined C_{2+} selectivity of ∼61% at 0.3 A cm^{-2}. This represents a 14% increase in C_2H_4 FE and approximately a 20% increase in combined C_{2+} selectivity relative to that of conventional Cu/ionomer. A maximum C_2H_4 partial current density of 139.5 mA cm^{-2} (J_{total} = 400 mA cm^{-2}) is obtained for Cu/polyionomer vs 116 mA cm^{-2} for Cu/ionomer (Figure 5b and Figure S21).

Single pass carbon utilization (SPCU) was performed at different flow rates at a fixed current density of 0.3 A cm^{-2} (Figure 5c). Decreasing the flow rate from 40 to 0.5 mL min^{-1} increased SPCU up to 84.0% (±1.6%) while maintaining a C_{2+} conversion of 64.8% (±4.1%). The corresponding FE evolution demonstrates stable product distribution over time (Figure S22). This represents one of the few systems achieving SPCU higher than 60% at application-relevant current densities (>0.2 A cm^{-2}) (Table S5). Compared with Cu/ionomer, this represents a 35% net improvement in carbon utilization (Figure 5d).

The combined C_{2+} partial current density and C_{2+} carbon utilization (j_{C2+}·CU), a proxy of product concentration in the outlet stream, shows an improvement of at least two times when compared with most Cu-based modified catalysts (Figure S23 and Table S5).

Under continuous operation at 0.1 A cm^{-2}, Cu/polyionomer sustained a C_2H_4 Faradaic efficiency of 23 ± 5% for nearly 24 h (Figure S24a). At 0.3 A cm^{-2} a higher FE (37 ± 3%) is sustained for 2 h (Figure S24b). Post-mortem scanning electron microscopy/energy dispersive X-ray (SEM/EDX) analysis revealed that such performance decay correlates with localized salt precipitation (Figure S25). XPS and Raman conducted after operation confirmed that both PEI and PFSA remain on the electrode surface (Figures S26 and S27). These findings point

https://doi.org/10.1021/jacs.5c01314
J. Am. Chem. Soc. 2025, 147, 27278−27288

toward salt crystallization and flooding as the main deactivation mechanism.

To extend the stability, we evaluated two complementary mitigation strategies. First, we explored pulsed electrolysis operation sequencing electrochemical reduction (on time) and chemical oxidation (off-time) as a means to reset the buildup of salt accumulation.[74−76] This led to a 4-fold improvement in stability, maintaining C_2H_4 production for at least 8 h (Figure 5e).

Alternatively, we explored the incorporation of a thin Vulcan-carbon layer atop the Cu/polyionomer, a common strategy to extend lifetime in CO_2R electrodes.[73] The addition of such a porous conductive layer may inhibit salt buildup directly over the catalyst surface, which in our case resulted in extended lifetime from ∼2 to ∼10 h of continuous electrolysis with similar FEs at 0.3 A cm^{-2} (Figure 5f and Figure S24b). This performance aligns with reported systems operating under acidic conditions at high current densities, where electrode lifetimes are generally limited and most systems demonstrate stability for 10 h or less (Table S5).

CONCLUSIONS

The electrochemical conversion of CO_2 to multicarbon products requires the combined advance in performance metrics that enable full process viability when considering CO_2 sourcing and product management (separation, purification, concentration). This is largely determined by the overall energy and carbon intensity, impacting costs and the environmental viability prospects. CO_2R in acid media is one strategy that could potentially overcome energy and carbon efficiency bottlenecks but is challenged by the competition with the hydrogen evolution reaction, and insufficient energy efficiency and stability.

We demonstrate a strategy that addresses selectivity and carbon utilization in acidic media based on catalyst environment control. We found that conventional environment manipulation based on PFSA ionomers such as Nafion resulted in a pH-sensitive structure−chemical function. This was evidenced by the change in hydrophobicity and carbon vs hydrogen selectivity with lowering pH. We then designed a polyionomer coating combining PFSA and polyethylenimine that, through the interaction of their functional groups, was able to lock chemical function down to lower pH, whose function is enhanced in acidic conditions. Using in situ Raman spectroscopy, we found that such a polyionomer coating buffers local protons and balances CO_2R intermediates, leading to improved selectivity toward C_{2+} products: with a multicarbon Faradaic efficiency of 61% and single-pass CO_2 utilization of 84%, including a conversion efficiency of 64% toward C_{2+} at a current density of 0.3 A cm^{-2}. This represents a net increase of nearly 30% in C_{2+} selectivity and 35% in carbon utilization compared to benchmark Cu/ionomer controls. The strategy presented herein offers new design handles to manipulate reaction microenvironments in electrochemical reactions and provides new ideas for future studies on the role of polyionomer structure in gas transport mechanisms by modeling atomic-level interactions over time to explain the experimentally observed improved selectivity and proton scavenging effect. Further progress would need to address the still prominent salt accumulation due to local OH^- formation and highly potassium concentrated electrolytes, leading to limited stability and energy efficiency. While the polyionomer strategy presented herein effectively controls proton availability and enhances C−C coupling, it does not resolve stability issues, underscoring the need for future work focused on extending operational lifetime alongside maintaining high selectivity and energy efficiency.

METHODS

Gas Diffusion Electrode Preparation. Cu electrodes, with 300 nm thickness, were prepared by sputtering pure Cu on top of a PTFE gas diffusion layer with a 450 nm pore size. Cu/ionomer, Cu/polymer, and Cu/polyionomer were fabricated by spray coating. For a 1:10 ratio of polymer:ionomer, the loading of Nafion (PFSA) (5 wt %, Sigma-Aldrich) was 10 μL cm^{-2} and PEI (0.28 μM aqueous solution, branched, Mw 25,000) was 1 μL cm^{-2}. They were dispersed in methanol (99.9%, Scharlau) and sonicated for at least 30 min before spray coating.

Gas Diffusion Electrode Characterization. *Contact angle*: measurements were performed using the sessile drop method on a video-based contact angle system (OCA 15EC). Data were collected in 3 different spots to get an average and standard deviation. *Attenuated total reflectance-Fourier transform infrared (ATR-FTIR)*: spectra were obtained from the electrodes by using an Agilent Cary 630 FTIR spectrometer in transmittance mode. *X-ray photoelectron spectroscopy (XPS)*: spectra were obtained by measuring the electrodes using a SPECS PHOIBOS 150. XPS data analysis and fitting were carried out using CasaXPS software. The binding energies of all peaks were corrected with respect to a C 1s peak (284.5 eV). *Scanning electron microscopy (SEM)* imaging was performed with a Zeiss Auriga Crossbeam. *Atomic Force Microscopy (AFM)* measurements were performed on a Park Systems NX10 under ambient conditions in noncontact mode. For electrical measurements, the specimens were mounted on a steel disk and electrically ground using conductive silver paste and copper tape (RS Components). *Topography and nanomechanical data*: Arrow-NCR probes (R = 8 nm, k = 42 N/m, f = 285 kHz) were used for the topography and nanomechanical maps. The deflection sensitivity was calibrated on a sapphire standard and the spring constant via the Sader method.[77] *Kelvin probe force microscopy (KPFM)*: Pt-Ir coated PPP-EFM probes (R = 25 nm, k = 2.8 N/m, f = 75 kHz) were employed for the work function mapping. The scan rates were maintained low at 0.2−0.3 Hz, which enabled the feedback control to keep a stable scan regime, reliably tracking larger topographic features.

Electrochemical Measurements. An electrochemical three-compartment flow cell (Figure S28) was used for all electrochemical tests. The cathode gas chamber had a volume of 2.16 cm^3 (1.2 × 1.2 × 1.5 cm), expanding to 2.5 cm^3 when including the outlet gas tube. The anode chamber had a volume of 1.3 cm^3 (1.2 × 1.2 × 0.9 cm). Electrochemical measurements were conducted using an Autolab 204.s workstation connected to a current booster in galvanostatic mode. The anolyte and catholyte were separated by a Nafion membrane 117. Cu/PTFE, Cu/ionomer, Cu/polymer, and Cu/polyionomer were used as cathode in different tests (electrode area of at least 1.5 cm^2). Ag/AgCl (3.5 M KCl) was used as a reference electrode. Electrode potentials were rescaled to the reversible hydrogen electrode (RHE) reference by

$$E_{RHE} = E_{Ag/AgCl} + 0.223\ V + 0.059 \times pH \quad (4)$$

For all measurements the anolyte was 0.5 M H_2SO_4 solution, and platinum mesh was used as the counter electrode. The electrolyte flow rate was 30 mL min^{-1}, achieved with a peristaltic pump. A CO_2 flow of 40 mL min^{-1} was employed for all measurements and controlled by a mass flow controller. 0.5 M K_2SO_4 was used as the catholyte, and the pH was adjusted using concentrated H_2SO_4 and checked with a pH meter. A constant volume of 20 mL was recirculated through anode and cathode compartments using peristaltic pumps. Each current was applied for at least 13 min based on prior reports.[78] This duration allowed for sufficient time for the liquid products to form, while also enabling a comprehensive measurement of the electrochemical response under stable conditions. SPCE was performed under a constant current density of 0.3 A cm^{-2} in a flow cell at various CO_2 flow rates and repeated at least three times to ensure reproducibility. Following the standard methodology of similar works assessing CO_2

https://doi.org/10.1021/jacs.5c01314
J. Am. Chem. Soc. 2025, 147, 27278−27288

electrolysis at flow rates, the outlet of the gas stream was immersed in a water reservoir to maintain a constant back pressure, preventing fluctuations that could influence mass transport or reaction kinetics. The measurement duration was adjusted in accordance with the internal volume of the gas chamber, allowing sufficient time for CO_2 to equilibrate and fully diffuse to the catalyst surface. This ensured that the observed conversion rates were representative of steady state conditions. Corresponding FE evolution demonstrates stable product distribution over time (Figure S22). Gas flow was monitored by using a calibrated mass flow controller. Stability measurement was performed with electrochemical CO_2 reduction at a fixed current densities of 0.1 A cm^{-2} and 0.3 A cm^{-2}, monitoring products over time. To overcome flooding issues, we applied two different strategies at 0.3 A cm^{-2}. (1) A layer of carbon nanoparticles (Vulcan XC72, actual loading ~0.2 mg/cm^2)[29] was placed atop the Cu/polyionomer and electrolyte flow decreased to 10 mL/min. Catholyte (anolyte) was exchanged with new solution after 5 h of operation, approximately. Salt accumulated at the cathode was periodically washed with Milli-Q water and N_2. (2) An alternating electrolysis sequence of on- and off-time (15 min) after first 1 h was used. *iR* correction was made considering the solution resistance determined using EIS in −0.3 V vs RHE. Gas products from CO_2R were analyzed using a gas chromatograph (PerkinElmer Clarus 590) coupled with a thermal conductivity detector (TCD) and a flame ionization detector (FID). Argon was used as the carrier gas. Tests were performed in triplicate. The Faradaic efficiency was calculated via

$$\text{Faradaic efficiency (\%, FE)} = \frac{n \times F \times V_m \times f_m}{J} \times 100 \quad (5)$$

where n is the number of electrons for a given product, F is the Faradaic constant, V_m is the molar volume, f_m is the molar reacting gas flow rate, and J is the current.

Single-pass CO_2 conversion efficiency (SPCU) of CO_2 was calculated using the equation

$$\text{SPCU (\%)} = \frac{\frac{j}{n \times F} \times V_m}{f_m} \quad (6)$$

where j represents the partial current density of a specific product, n represents the number of electrons required for the specific product, F represents the Faraday constant, V_m represents the molar volume, and f_m is the molar reacting gas flow rate.

Liquid products were analyzed by using ^{1}H NMR (Bruker 500 MHz) spectroscopy with water suppression. We used dimethyl sulfoxide (DMSO) as the reference standard and deuterium oxide (D_2O) as the lock solvent.

***In Situ* Raman Spectroscopy Measurements.** *In situ* Raman spectroscopy were measured by Renishaw with a custom-made in situ cell by an immersion objective (L63x) covered with PFA film using a 785 nm excitation laser equipped with 1800 I/mm grating. The samples measured were Cu/PTFE, Cu/ionomer, Cu/polymer, and Cu/polyionomer. The samples were prepared by spray coating and the loading of ionomer was 10 μL cm^{-2} and 1 μL cm^{-2} of polymer, respectively. The potentials were applied by a single channel Autolab204 potentiostat using 0.5 M K_2SO_4 (pH 2) as electrolyte, Pt wire as counter electrode, and Ag/AgCl (3 M KCl) as reference electrode. All the data were acquired by 0.1% laser power with 2 s of laser exposure with 30 accumulations.

■ ASSOCIATED CONTENT

Supporting Information

The Supporting Information is available free of charge at https://pubs.acs.org/doi/10.1021/jacs.5c01314.

Additional electrochemical and characterization analysis, detailed pH study results, additional *in situ* Raman spectra, CO_2R product distribution and stability, and electrochemical flow cell setup (PDF)

■ AUTHOR INFORMATION

Corresponding Author

F. Pelayo García de Arquer − *ICFO-Institut de Ciències Fotòniques, The Barcelona Institute of Science and Technology, Castelldefels (Barcelona) 08860, Spain;* orcid.org/0000-0003-2422-6234; Email: pelayo.garciadearquer@icfo.eu

Authors

Bárbara Polesso − *ICFO-Institut de Ciències Fotòniques, The Barcelona Institute of Science and Technology, Castelldefels (Barcelona) 08860, Spain;* orcid.org/0000-0003-4722-7491

Adrián Pinilla-Sánchez − *ICFO-Institut de Ciències Fotòniques, The Barcelona Institute of Science and Technology, Castelldefels (Barcelona) 08860, Spain*

Eman H. Ahmed − *ICFO-Institut de Ciències Fotòniques, The Barcelona Institute of Science and Technology, Castelldefels (Barcelona) 08860, Spain; NRC-National Research Centre, Polymers and Pigments Department, Chemical industries research institute, Advanced Materials and Nanotechnology group, Cairo 12622, Egypt*

Anku Guha − *ICFO-Institut de Ciències Fotòniques, The Barcelona Institute of Science and Technology, Castelldefels (Barcelona) 08860, Spain*

Marinos Dimitropoulos − *ICFO-Institut de Ciències Fotòniques, The Barcelona Institute of Science and Technology, Castelldefels (Barcelona) 08860, Spain;* orcid.org/0000-0002-1466-4575

Blanca Belsa − *ICFO-Institut de Ciències Fotòniques, The Barcelona Institute of Science and Technology, Castelldefels (Barcelona) 08860, Spain;* orcid.org/0000-0002-9256-8714

Viktoria Golovanova − *ICFO-Institut de Ciències Fotòniques, The Barcelona Institute of Science and Technology, Castelldefels (Barcelona) 08860, Spain*

Lu Xia − *ICFO-Institut de Ciències Fotòniques, The Barcelona Institute of Science and Technology, Castelldefels (Barcelona) 08860, Spain;* orcid.org/0000-0002-2726-5389

Ranit Ram − *ICFO-Institut de Ciències Fotòniques, The Barcelona Institute of Science and Technology, Castelldefels (Barcelona) 08860, Spain;* orcid.org/0000-0002-7999-5551

Sunil Kadam − *ICFO-Institut de Ciències Fotòniques, The Barcelona Institute of Science and Technology, Castelldefels (Barcelona) 08860, Spain*

Aparna M. Das − *ICFO-Institut de Ciències Fotòniques, The Barcelona Institute of Science and Technology, Castelldefels (Barcelona) 08860, Spain*

Junmei Chen − *ICFO-Institut de Ciències Fotòniques, The Barcelona Institute of Science and Technology, Castelldefels (Barcelona) 08860, Spain*

Johann Osmond − *ICFO-Institut de Ciències Fotòniques, The Barcelona Institute of Science and Technology, Castelldefels (Barcelona) 08860, Spain*

Adam Radek Martínez − *ICFO-Institut de Ciències Fotòniques, The Barcelona Institute of Science and Technology, Castelldefels (Barcelona) 08860, Spain*

Melanie Micali − *Center for Nanophotonics, NWO-Institute AMOLF, 1098 XG Amsterdam, The Netherlands*

Esther Alarcón Lladó − *Center for Nanophotonics, NWO-Institute AMOLF, 1098 XG Amsterdam, The Netherlands; Van't Hoff Institute for Molecular Sciences (HIMS), University*

https://doi.org/10.1021/jacs.5c01314
J. Am. Chem. Soc. 2025, 147, 27278−27288

of Amsterdam, 1090 GD Amsterdam, The Netherlands;
orcid.org/0000-0001-7317-9863

Complete contact information is available at:
https://pubs.acs.org/10.1021/jacs.5c01314

Notes

The authors declare no competing financial interest.

■ ACKNOWLEDGMENTS

ICFO thanks the Fundació Cellex, Fundació Mir-Puig, Generalitat de Catalunya (SGR 01455); the La Caixa Foundation (100010434, E.U. Horizon 2020 Marie Skłodowska-Curie grant agreement 847648); the European Union (NASCENT, 101077243); and PID2022-138127NA-I00 funded by MCIN/AEI/10.13039/501100011033/. A.P.-S. acknowledges PRE2021-098995 and FSE+. E.H.A. acknowledges Women for Africa foundation, 7th edition science by women program. A.G. acknowledges JDC2023-052976-I. B.B. acknowledges MCIN/AEI/10.13039/501100011033539 and FSE [PRE2019-088522]. V.G. acknowledges the Severo Ochoa Excellence Postdoctoral Fellowship [CEX2019-000910-S]. The work of E.A.L. and M.M. is part of the Dutch Research Council (NWO) and EU Pathfinder project SolarUP.

■ REFERENCES

(1) Kibria, M. G.; et al. Electrochemical CO_2 Reduction into Chemical Feedstocks: From Mechanistic Electrocatalysis Models to System Design. *Adv. Mater.* **2019**, *31*, 1807166.
(2) Langie, K. M. G.; et al. Toward economical application of carbon capture and utilization technology with near-zero carbon emission. *Nat. Commun.* **2022**, *13*, 1−10.
(3) Dinh, C. T.; et al. CO_2 electroreduction to ethylene via hydroxide-mediated copper catalysis at an abrupt interface. *Science.* **2018**, *360*, 783−787.
(4) De Luna, P. What would it take for renewably powered electrosynthesis to displace petrochemical processes? *Science* **2019**, *364*, 1.
(5) Nitopi, S.; et al. Progress and Perspectives of Electrochemical CO_2 Reduction on Copper in Aqueous Electrolyte. *Chem. Rev.* **2019**, *119*, 7610−7672.
(6) Stephens, I. E. L.; et al. 2022 roadmap on low temperature electrochemical CO_2 reduction. *J. Phys. Energy* **2022**, *4*, 042003.
(7) Khoo, H. H.; Halim, I.; Handoko, A. D. LCA of electrochemical reduction of CO_2 to ethylene. *J. CO2 Util.* **2020**, *41*, 101229.
(8) Ruiz-López, E.; Gandara-Loe, J.; Baena-Moreno, F.; Reina, T. R.; Odriozola, J. A. Electrocatalytic CO_2 conversion to C_2 products: Catalysts design, market perspectives and techno-economic aspects. *Renewable and Sustainable Energy Reviews* **2022**, *161*, 112329.
(9) García de Arquer, F. P.; et al. CO_2 electrolysis to multicarbon products at activities greater than 1 A cm^{-2}. *Science.* **2020**, *367*, 661−666.
(10) Zheng, M.; et al. Electrocatalytic CO_2-to-C_{2+} with Ampere-Level Current on Heteroatom-Engineered Copper via Tuning *CO Intermediate Coverage. *J. Am. Chem. Soc.* **2022**, *144*, 14936−14944.
(11) Ma, W.; et al. Electrocatalytic reduction of CO_2 to ethylene and ethanol through hydrogen-assisted C-C coupling over fluorine-modified copper. *Nat. Catal.* **2020**, *3*, 478−487.
(12) Choi, C.; et al. Highly active and stable stepped Cu surface for enhanced electrochemical CO_2 reduction to C2H4. *Nat. Catal. 2020 310* **2020**, *3*, 804−812.
(13) Xie, Y.; et al. High carbon utilization in CO_2 reduction to multi-carbon products in acidic media. *Nat. Catal. 2022 56* **2022**, *5*, 564−570.
(14) Huang, J. E.; et al. CO2 electrolysis to multicarbon products in strong acid. *Science.* **2021**, *372*, 1074−1078.
(15) Zhang, L.; et al. Atomically Dispersed Ni-Cu Catalysts for pH-Universal CO_2 Electroreduction. *Adv. Mater.* **2023**, *35*, 1−10.
(16) Ozden, A.; et al. Energy- and carbon-efficient CO_2/CO electrolysis to multicarbon products via asymmetric ion migration-adsorption. *Nat. Energy* **2023**, *8*, 179−190.
(17) Gabardo, C. M.; et al. Continuous Carbon Dioxide Electroreduction to Concentrated Multi-carbon Products Using a Membrane Electrode Assembly. *Joule* **2019**, *3*, 2777−2791.
(18) Ozden, A.; et al. Cascade CO_2 electroreduction enables efficient carbonate-free production of ethylene. *Joule* **2021**, *5*, 706−719.
(19) Wei, P.; et al. Coverage-driven selectivity switch from ethylene to acetate in high-rate CO_2/CO electrolysis. *Nat. Nanotechnol. 2023 183* **2023**, *18*, 299−306.
(20) Oener, S. Z.; Foster, M. J.; Boettcher, S. W. Accelerating water dissociation in bipolar membranes and for electrocatalysis. *Science (80-.).* **2020**, *369*, 1099−1103.
(21) Zhao, Y.; et al. Conversion of CO_2 to multicarbon products in strong acid by controlling the catalyst microenvironment. *Nat. Synth.* **2023**, *2*, 403−412.
(22) Gu, J.; et al. Modulating electric field distribution by alkali cations for CO_2 electroreduction in strongly acidic medium. *Nat. Catal.* **2022**, *5*, 268−276.
(23) Fan, M.; et al. Single-site decorated copper enables energy- and carbon-efficient CO_2 methanation in acidic conditions. *Nat. Commun.* **2023**, *14*, 1−8.
(24) Vichou, E.; et al. Tuning Selectivity of Acidic Carbon Dioxide Electrolysis via Surface Modification. *Chem. Mater.* **2023**, *35*, 7060−7068.
(25) Zhang, T. Acidic CO_2 Electrolysis Addressing the "Alkalinity Issue" and Achieving High CO_2 Utilization. *Chem. - A Eur. J.* **2023**, *29*, e202301455.
(26) Ma, Z.; et al. CO_2 electroreduction to multicarbon products in strongly acidic electrolyte via synergistically modulating the local microenvironment. *Nat. Commun.* **2022**, *13*, 1−11.
(27) O'Brien, C. P.; et al. Single Pass CO_2 Conversion Exceeding 85% in the Electrosynthesis of Multicarbon Products via Local CO_2 Regeneration. *ACS Energy Lett.* **2021**, *6*, 2952−2959.
(28) Xie, Y.; et al. High carbon utilization in CO_2 reduction to multi-carbon products in acidic media. *Nat. Catal.* **2022**, *5*, 564−570.
(29) Fan, M.; et al. Cationic-group-functionalized electrocatalysts enable stable acidic CO_2 electrolysis. *Nat. Catal.* **2023**, *6*, 763−772.
(30) Song, D.; et al. Electrochemical CO_2 reduction catalyzed by organic/inorganic hybrids. *eScience* **2023**, *3*, 100097.
(31) Nie, W.; Heim, G. P.; Watkins, N. B.; Agapie, T.; Peters, J. C. Organic Additive-derived Films on Cu Electrodes Promote Electrochemical CO_2 Reduction to C_{2+} Products Under Strongly Acidic Conditions. *Angew. Chemie Int. Ed.* **2023**, *62*, No. e202216102.
(32) Bouraada, M.; Ouali, M. S.; de Ménorval, L. C. Dodecylsulfate and dodecybenzenesulfonate intercalated hydrotalcites as adsorbent materials for the removal of BBR acid dye from aqueous solutions. *J. Saudi Chem. Soc.* **2016**, *20*, 397−404.
(33) Fang, M.; et al. Anionic Ionomer: Released Surface-Immobilized Cations and an Established Hydrophobic Microenvironment for Efficient and Durable CO_2-to-Ethylene Electrosynthesis at High Current over One Month. *J. Am. Chem. Soc.* **2024**, *146*, 27060−27069.
(34) Wu, W.; et al. Addressing the Carbonate Issue: Electrocatalysts for Acidic CO_2 Reduction Reaction. *Adv. Mater.* **2025**, *37*, 2312894.
(35) Chen, X.; et al. Electrochemical CO_2-to-ethylene conversion on polyamine-incorporated Cu electrodes. *Nat. Catal. 2020 41* **2021**, *4*, 20−27.
(36) Wang, H. K.; Sit, C. Y.; Haasch, R. T.; Kenis, P. J. A.; Gewirth, A. A. Effect of Polymer Variation in Cu-Polymer Composite Electrodes on Electrochemical CO_2 Reduction. *ACS Appl. Energy Mater.* **2025**, *8*, 2993.
(37) Wang, Y.; et al. Enhancing CO_2 Electroreduction to Multicarbon Products by Modulating the Surface Microenvironment of Electrode with Polyethylene Glycol. *Angew. Chemie Int. Ed.* **2025**, *64*, No. e202420661.
(38) Kim, C.; et al. Tailored catalyst microenvironments for CO_2 electroreduction to multicarbon products on copper using bilayer ionomer coatings. *Nat. Energy 2021 611* **2021**, *6*, 1026−1034.

(39) Chen, J.; et al. Selective and stable CO_2 electroreduction at high rates via control of local H_2O/CO_2 ratio. *Nat. Commun.* **2024**, *15*, 5893.
(40) Watkins, N. B.; Wu, Y.; Nie, W.; Peters, J. C.; Agapie, T. In Situ Deposited Polyaromatic Layer Generates Robust Copper Catalyst for Selective Electrochemical CO_2 Reduction at Variable pH. *ACS Energy Lett.* **2023**, *8*, 189−195.
(41) Guzmán, J.; Saucedo, I.; Navarro, R.; Revilla, J.; Guibal, E. Vanadium interactions with chitosan: Influence of polymer protonation and metal speciation. *Langmuir* **2002**, *18*, 1567−1573.
(42) Bahulekar, R.; Ayyangar, N. R.; Ponrathnam, S. Polyethyleneimine in immobilization of biocatalysts. *Enzyme Microb. Technol.* **1991**, *13*, 858−868.
(43) Singh, S.; Taketsugu, T.; Singh, R. K. Hydration, Prediction of the pKa, and Infrared Spectroscopic Study of Sulfonated Polybenzophenone (SPK) Block-Copolymer Hydrocarbon Membranes and Comparisons with Nafion. *ACS Omega* **2021**, *6*, 32739−32748.
(44) Feng, S.; et al. Effect of poly(ethylene glycol) molecular weight on CO_2/N_2 separation performance of poly(amide-12-b-ethylene oxide)/poly(ethylene glycol) blend membranes. *J. Energy Chem.* **2019**, *28*, 39−45.
(45) Joseph, J.; Tseng, C. Y.; Hwang, B. J. Phosphonic acid-grafted mesostructured silica/Nafion hybrid membranes for fuel cell applications. *J. Power Sources* **2011**, *196*, 7363−7371.
(46) Krupina, A. A.; Kayumov, R. R.; Nechaev, G. V.; Lapshin, A. N.; Shmygleva, L. V. Polymer Electrolytes Based on Na-Nafion Plasticized by Binary Mixture of Ethylene Carbonate and Sulfolane. *Membranes.* **2022**, *12*, 840.
(47) Ghazali, Z.; et al. Impregnating deep eutectic solvent choline chloride:urea:polyethyleneimine onto mesoporous silica gel for carbon dioxide capture. *J. Mater. Res. Technol.* **2020**, *9*, 3249−3260.
(48) Kusoglu, A.; Weber, A. Z. New Insights into Perfluorinated Sulfonic-Acid Ionomers. *Chem. Rev.* **2017**, *117*, 987−1104.
(49) Wu, Z. Z.; Gao, F. Y.; Gao, M. R. Regulating the oxidation state of nanomaterials for electrocatalytic CO_2 reduction. *Energy Environ. Sci.* **2021**, *14*, 1121−1139.
(50) Liu, T.; et al. Improving Interfacial Electron Transfer via Tuning Work Function of Electrodes for Electrocatalysis: From Theory to Experiment. *J. Phys. Chem. C* **2019**, *123*, 28319−28326.
(51) Deng, W.; et al. Unraveling the rate-determining step of C_{2+} products during electrochemical CO reduction. *Nat. Commun. 2024 151* **2024**, *15*, 1−8.
(52) Ruqia, B.; et al. Recent advances in the electrochemical CO reduction reaction towards highly selective formation of C_x products (X = 1−3). *Chem. Catal.* **2022**, *2*, 1961−1988.
(53) Zhan, C.; et al. Revealing the CO Coverage-Driven C-C Coupling Mechanism for Electrochemical CO_2 Reduction on Cu_2O Nanocubesvia Operando Raman Spectroscopy. *ACS Catal.* **2021**, *11*, 7694−7701.
(54) Li, F.; et al. Molecular tuning of CO_2-to-ethylene conversion. *Nature* **2020**, *577*, 509−513.
(55) Li, Y. C.; et al. Binding Site Diversity Promotes CO_2 Electroreduction to Ethanol. *J. Am. Chem. Soc.* **2019**, *141*, 8584−8591.
(56) Zhan, C. Key intermediates and Cu active sites for CO_2 electroreduction to ethylene and ethanol. *Nat. Energy* **2024**, *9*, 1485.
(57) Moradzaman, M.; Mul, G. In Situ Raman Study of Potential-Dependent Surface Adsorbed Carbonate, CO, OH, and C Species on Cu Electrodes During Electrochemical Reduction of CO_2. *ChemElectroChem* **2021**, *8*, 1478.
(58) De Ruiter, J.; et al. Probing the Dynamics of Low-Overpotential CO_2-to-CO Activation on Copper Electrodes with Time-Resolved Raman Spectroscopy. *J. Am. Chem. Soc.* **2022**, *144*, 15047−15058.
(59) Zhao, Y.; et al. Elucidating electrochemical CO_2 reduction reaction processes on Cu(hkl) single-crystal surfaces by in situ Raman spectroscopy. *Energy Environ. Sci.* **2022**, *15*, 3968−3977.
(60) An, H.; et al. Spatiotemporal Mapping of Local Heterogeneities during Electrochemical Carbon Dioxide Reduction. *JACS Au* **2023**, *3*, 1890−1901.
(61) Li, F.; et al. Molecular tuning of CO_2-to-ethylene conversion. *Nature* **2020**, *577*, 509−513.
(62) Qu, J.; et al. Electrochemical Carbon Dioxide Reduction to Ethylene: From Mechanistic Understanding to Catalyst Surface Engineering. *Nano-Micro Lett.* **2023**, *15*, 1−34.
(63) Zhai, Y.; Chuang, S. S. C. Enhancing Degradation Resistance of Polyethylenimine for CO_2 Capture with Cross-Linked Poly(vinyl alcohol). *Ind. Eng. Chem. Res.* **2017**, *56*, 13766−13775.
(64) Yu, F.; et al. Electrochemical CO_2 reduction: From catalysts to reactive thermodynamics and kinetics. *Carbon Capture Sci. Technol.* **2023**, *6*, 100081.
(65) Monteiro, M. C. O.; Dattila, F.; López, N.; Koper, M. T. M. The Role of Cation Acidity on the Competition between Hydrogen Evolution and CO_2 Reduction on Gold Electrodes. *J. Am. Chem. Soc.* **2022**, *144*, 1589−1602.
(66) Park, J.; et al. Strategies for CO_2 electroreduction in cation exchange membrane electrode assembly. *Chem. Eng. J.* **2023**, *453*, 139826.
(67) Monteiro, M. C. O.; et al. Time-Resolved Local pH Measurements during CO_2 Reduction Using Scanning Electrochemical Microscopy: Buffering and Tip Effects. *JACS Au* **2021**, *1*, 1915−1924.
(68) Monteiro, M. C. O.; Philips, M. F.; Schouten, K. J. P.; Koper, M. T. M. Efficiency and selectivity of CO_2 reduction to CO on gold gas diffusion electrodes in acidic media. *Nat. Commun.* **2021**, *12*, 1−7.
(69) Bondue, C. J.; Graf, M.; Goyal, A.; Koper, M. T. M. Suppression of Hydrogen Evolution in Acidic Electrolytes by Electrochemical CO_2 Reduction. *J. Am. Chem. Soc.* **2021**, *143*, 279−285.
(70) Ringe, S. Double layer charging driven carbon dioxide adsorption limits the rate of electrochemical carbon dioxide reduction on Gold. *Nat. Commun.* **2020**, *11*, 33.
(71) Jiang, X.; Li, H.; Yang, Y.; Gao, D. pH dependence of CO_2 electroreduction selectivity over size-selected Au nanoparticles. *J. Mater. Sci.* **2020**, *55*, 13916−13926.
(72) Wang, L.; et al. Electrochemical Carbon Monoxide Reduction on Polycrystalline Copper: Effects of Potential, Pressure, and pH on Selectivity toward Multicarbon and Oxygenated Products. *ACS Catal.* **2018**, *8*, 7445−7454.
(73) Yang, K.; Kas, R.; Smith, W. A.; Burdyny, T. Role of the Carbon-Based Gas Diffusion Layer on Flooding in a Gas Diffusion Electrode Cell for Electrochemical CO2Reduction. *ACS Energy Lett.* **2021**, *6*, 33−40.
(74) Nguyen, T. N.; et al. Catalyst Regeneration via Chemical Oxidation Enables Long-Term Electrochemical Carbon Dioxide Reduction. *J. Am. Chem. Soc.* **2022**, *144*, 13254−13265.
(75) Xu, Y.; et al. Self-Cleaning CO_2 Reduction Systems: Unsteady Electrochemical Forcing Enables Stability. *ACS Energy Lett.* **2021**, *6*, 809−815.
(76) Zhang, X. Da; et al. Asymmetric Low-Frequency Pulsed Strategy Enables Ultralong CO_2 Reduction Stability and Controllable Product Selectivity. *J. Am. Chem. Soc.* **2023**, *145*, 2195−2206.
(77) Sader, J. E.; et al. A virtual instrument to standardise the calibration of atomic force microscope cantilevers. *Rev. Sci. Instrum.* **2016**, *87*, 93711.
(78) Chang, M.; Ren, W.; Ni, W.; Lee, S.; Hu, X. Ionomers Modify the Selectivity of Cu-Catalyzed Electrochemical CO_2 Reduction. *ChemSusChem* **2023**, *16*, No. e202201687.

https://doi.org/10.1021/jacs.5c01314
J. Am. Chem. Soc. 2025, 147, 27278−27288